Eur J Nucl Med Mol Imaging (2013) 40:744–758
DOI 10.1007/s00259-012-2326-2

ORIGINAL ARTICLE

Performance evaluation of small-animal multipinhole μSPECT scanners for mouse imaging

Steven Deleye · Roel Van Holen · Jeroen Verhaeghe · Stefaan Vandenberghe · Sigrid Stroobants · Steven Staelens

Received: 3 August 2012 / Accepted: 12 December 2012 / Published online: 24 January 2013

Abstract
Purpose We compared the performance of three commercial small-animal μSPECT scanners equipped with multipinhole general purpose (GP) and multipinhole high-resolution (HR) collimators designed for imaging mice.
Methods Spatial resolution, image uniformity, point source sensitivity and contrast recovery were determined for the U-SPECT-II (MILabs), the NanoSPECT-NSO (BioScan) and the X-SPECT (GE) scanners. The pinhole diameters of the HR collimator were 0.35 mm, 0.6 mm and 0.5 mm for these three systems respectively. A pinhole diameter of 1 mm was used for the GP collimator. To cover a broad field of imaging applications three isotopes were used with various photon energies: ^{99m}Tc (140 keV), ^{111}In (171 and 245 keV) and ^{125}I (27 keV). Spatial resolution and reconstructed image uniformity were evaluated in both HR and a GP mode with hot rod phantoms, line sources and a uniform phantom. Point source sensitivity and contrast recovery measures were additionally obtained in the GP mode with a novel contrast recovery phantom developed in-house containing hot and cold submillimetre capillaries on a warm background.
Results In hot rod phantom images, capillaries as small as 0.4 mm with the U-SPECT-II, 0.75 mm with the X-SPECT and 0.6 mm with the NanoSPECT-NSO could be resolved with the HR collimators for ^{99m}Tc. The NanoSPECT-NSO achieved this resolution in a smaller field-of-view (FOV) and line source measurements showed that this device had a lower axial than transaxial resolution. For all systems, the degradation in image resolution was only minor when acquiring the more challenging isotopes ^{111}In and ^{125}I. The point source sensitivity with ^{99m}Tc and GP collimators was 3,984 cps/MBq for the U-SPECT-II, 620 cps/MBq for the X-SPECT and 751 cps/MBq for the NanoSPECT-NSO. The effects of volume sensitivity over a larger object were evaluated by measuring the contrast recovery phantom in a realistic FOV and acquisition time. For 1.5-mm rods at a noise level of 8 %, the contrast recovery coefficient (CRC) was 42 %, 37 % and 34 % for the U-SPECT-II, X-SPECT and NanoSPECT-NSO, respectively. At maximal noise levels of 10 %, a CRC_{cold} of 70 %, 52 % and 42 % were obtained for the U-SPECT-II, X-SPECT and NanoSPECT-NSO, respectively. When acquiring ^{99m}Tc with the GP collimators, the integral/differential uniformity values were 30 %/14 % for the U-SPECT-II, 50 %/30 % for the X-SPECT and 38 %/25 % for the NanoSPECT-NSO. When using the HR collimators, these uniformity values remained similar for U-SPECT-II and X-SPECT, but not for the NanoSPECT-NSO for which the uniformity deteriorated with larger volumes.
Conclusion We compared three μSPECT systems by acquiring and analysing mouse-sized phantoms including a

S. Deleye (✉) · J. Verhaeghe · S. Stroobants · S. Staelens
Molecular Imaging Center Antwerp, Antwerp University,
Universiteitsplein 1,
2610 Antwerp, Belgium
e-mail: steven.deleye@ua.ac.be

S. Stroobants
Nuclear Medicine Department, University Hospital Antwerp,
Wilrijkstraat 10,
2650 Antwerp, Belgium

R. Van Holen · S. Vandenberghe
Department of Electronics and Information Systems,
MEDISIP-iMinds, Ghent University, De Pintelaan 185,
9000 Ghent, Belgium

contrast recovery phantom built in-house offering the ability to measure the hot contrast on a warm background in the submillimetre resolution range. We believe our evaluation addressed the differences in imaging potential for each system to realistically image tracer distributions in mouse-sized objects.

Keywords Small-animal imaging · SPECT · Pinhole · Multipinhole

Introduction

Molecular imaging is the visualization, characterization and measurement of biological processes at the molecular and cellular levels in humans and other living beings [1]. Molecular imaging instrumentation consists of a variety of modalities that are nowadays often combined in multimodal imaging systems: SPECT (single photon emission computed tomography), PET (positron emission tomography), optical imaging, MRI (magnetic resonance imaging), MRS (magnetic resonance spectroscopy) and US (ultrasonography). Compared to techniques such as autoradiography and microscopy, the possibility of studying small animals longitudinally in vivo justifies the need for molecular imaging. Functional molecular imaging studies usually assess the spatial distribution of administered exogenous molecules and expression levels of their target (mostly enzymes and receptors). These imaging biomarkers can provide a certain degree of contrast by specifically binding to a target at an exquisite sensitivity in the picomolar range [2].

The use of extrinsic collimation to derive the direction of the photons hampers the overall sensitivity of SPECT compared to that of PET, which is based on electronic coincidence counting to gather spatial information. Therefore in SPECT, one needs to find an optimum between imaging time, injected dose and image noise. On the other hand, the spatial resolution of μSPECT is much higher since there is no physical lower limit caused by positron range (which can be reasonably high for some positron emitters, e.g. mean 0.6 mm for ^{18}F in water [3]) and photon acolinearity as is the case in μPET. Also, parallax (depth-of-interaction effects) in the detector, which is the dominant factor in the resolution loss of PET, is much smaller in SPECT due to its lower photon energy. Moreover in μSPECT, these depth-of-interaction effects are usually reduced by pinhole magnification (typically by a factor of 3 to 12). While PET is able to follow the distribution of radiolabelled synthetic molecules with exquisite sensitivity, the relatively short half-lives of the common positron emitters ^{11}C (20 min) and ^{18}F (109 min) make them less suited to radiolabelling endogenous biomolecules. Due to their relatively large size, peptides and antibodies diffuse slowly into tissue, particularly if obstacles such as the blood–brain barrier reduce the delivery rate, and have relatively slow clearance from blood. In imaging studies, this may require hours or days for localization and washout from blood to achieve acceptable target to background levels. The time required for localization and blood clearance favours isotopes with longer half-lives such as the single photon emitters ^{99m}Tc (6.02 h), ^{123}I (13.2 h) and ^{111}In (2.8 days). Technetium, indium and iodine also have good chemical properties in binding biological compounds and do not require a cyclotron close by, which reduces costs. Although clinical PET imaging nowadays often outperforms SPECT in terms of image quality, the contrary is true for the preclinical arena. Here, the significantly higher resolution, although in a smaller field-of-view (FOV), of multipinhole SPECT compared to μPET is in many cases essential when imaging small animals, especially mice.

Small-animal SPECT systems are not merely scaled down versions of their clinical counterparts, but make use of dedicated multipinhole collimators. As a consequence of the pinhole magnification, measuring with a pinhole collimator can yield a reconstructed spatial resolution that is better than the detector's intrinsic spatial resolution. However, a small pinhole results in reduced the sensitivity, which has to be counteracted to avoid high injected activities or excessive acquisition times. While the first generation of systems were still manufactured with a single pinhole [4–7] in combination with a conventional gamma camera requiring long scan times (about 1 h) and high doses (>1 mCi), systems are now built with multiple pinhole collimators [8–13]. Current small-animal systems have detectors that rotate combined with axial bed translation, or have stationary detectors and bed translation in XYZ directions to extend the FOV up to the entire animal's body. Examples of such designs are, amongst others, the A-SPECT [6], the HiSPECT [14], the T-SPECT [15], the SemiSPECT [16], the FAST-SPECT [17], the U-SPECT-II, the NanoSPECT and the X-SPECT. A more extensive overview of pinhole imaging has been provided by Beekman and van der Have [18].

To provide multimodality imaging, SPECT systems are nowadays combined with an integrated CT scanner, which is placed behind or within the gantry of the SPECT imager. The most important application is to localize activity in the anatomical framework provided by CT. The CT information can also be used to perform partial volume, scatter and attenuation correction for improved tracer quantification [19]. SPECT has already been used as a tool in a broad range of applications: cardiovascular imaging [20, 21], imaging gene expression [22], oncology [23, 24], bone metabolism [25], neuroimaging [26] and inflammation [27], amongst other fields.

Imaging techniques are increasingly being applied to more challenging questions that relate to multiple molecular pathways in the body. Thus, the ability of SPECT to simultaneously acquire separate images of different molecules, enabling the resolution of the temporal relationship between different biological processes has become more important. This cannot be ensured with sequential studies when there is a rapidly changing pathophysiology. Imaging multiple molecular pathways at the same time can be solved by multi-isotope imaging in SPECT or the use of another collimator for simultaneous μPET and μSPECT [28].

We evaluated and compared the performance of the three most widely used state-of-the-art μSPECT systems for small-animal imaging: the U-SPECT-II (MILabs), the NanoSPECT (Bioscan) and the X-SPECT (GE). The evaluation criteria used in our comparison were reconstructed spatial resolution, sensitivity, contrast recovery and image uniformity for different isotopes (^{99m}Tc, ^{125}I and ^{111}In). These evaluations were performed for high-resolution (HR) and general purpose (GP) collimators, and involved mouse-sized phantoms.

Materials and methods

To obtain objective and representative data samples, measurements were performed in five different imaging facilities: the University of Ghent, Belgium (X-SPECT), the University of Florence, Italy (X-SPECT), the University Medical Center Utrecht, The Netherlands (U-SPECT-II), Radboud University Nijmegen, The Netherlands (U-SPECT-II) and Queen Mary University London, UK (NanoSPECT-NSO).

System descriptions

The main difference among the systems under evaluation was that in one camera (U-SPECT-II) the detectors are stationary, while in the others (NanoSPECT-NSO and X-SPECT) a gantry rotates around the object. A stationary system does not need rotation of heavy detectors and the only moving part is an XYZ stage that is also used for system matrix measurement [29, 30] obviating the need to perform geometric parameter calibration. The X-SPECT and the NanoSPECT-NSO have an adjustable radius of rotation (ROR) to adjust the magnification and a FOV for each specific imaging task. The U-SPECT-II on the other hand uses cylindrical collimators with different sizes and imaging FOV for rats and mice in order to maximize the count yield for the task at hand [31]. Furthermore, there is also a difference in the overlap of the projections. The U-SPECT-II makes use of detectors for which the projections do not overlap, while the NanoSPECT-NSO and the X-SPECT make use of projection multiplexing. While multiplexing increases the sensitivity, it also creates ambiguity during image reconstruction [32–34]. It has been reported that artifacts leading to, for example, image nonuniformities and 'ghost activity' can be attributed to this ambiguity [32]. The effects of multiplexing depend on the activity distribution, and also on the pinhole design, detector size and imaging distance.

U-SPECT-II

The U-SPECT-II system (Fig. 1a) has three detectors similar to a clinical triple headed SPECT system, resulting in a triangular shape. Each detector has a 9.5-mm thick crystal (NaI(Tl)) with an active detector area of 50.8×38.1 cm optically coupled through a light guide to 55 photomultiplier tubes (PMTs). The energy resolution is 10 % for ^{99m}Tc at 140 keV. The large detectors allow high pinhole magnification factors, which reduce the effects of low intrinsic detector resolution (3–4 mm) on the total system resolution. The total detector surface area is 5,806 cm^2. Projections are discretized using a pixel size of 1×1 mm. Before reaching the detectors the photons first need to pass the 75-pinhole collimator in a configuration of five rings with 15 pinholes per ring. This provides sufficient sampling in a small region such that there is no need for rotation of either the object or the detector. However, the small FOV requires the animal bed to be translated in three dimensions for whole-body (WB) acquisitions, which is called the scanning focus method and combines the scanning of multiple focus positions with the simultaneous reconstruction of all the projection data [35]. Also, the number of bed positions can be reduced when using spiral trajectories on the U-SPECT-II [36]. Around the pinholes of the mouse collimators there is a tungsten tube with 75 rectangular holes to prevent overlap of the projections. We used the 0.35, 0.6 and 1 mm aperture size collimator tubes. A more detailed description of the system has been provided by van der Have et al. [37], and a selection of user applications with the U-SPECT-II have been described [38–46].

X-SPECT

The X-SPECT system (Fig. 1b), as part of the Triumph (SPECT/PET/CT) system in its most complete configuration, has four rotating gamma camera heads (a configuration with one camera head was used in this study with compensation in phantom acquisition times) and is mounted on the same axial location of the gantry as the CT tube and X-ray detector. The camera consists of 5 × 5 CZT (CdZnTe) modules each made up of 16 × 16 pixel arrays of 1.5 mm square giving a total of 80 × 80 pixels and an active detector area of 12.7×12.7 cm^2. The pixelated detector thus has a 1.5-mm intrinsic (discrete) resolution and 5 % energy

Fig. 1 Commercially available small-animal SPECT systems evaluated in this study: **a** U-SPECT-II, **b** X-SPECT, **c** NanoSPECT-NSO

resolution at 140 keV. Each gamma camera head can be equipped with interchangeable single, multipinhole (five) [47] or parallel-hole collimators. In this study, we used only the 0.5-mm and 1.0-mm multipinhole collimators. A selection of user applications with the X-SPECT can be found in the literature [48, 49].

NanoSPECT-NSO

The NanoSPECT-NSO system (Fig. 1c) consists in its most complete form of four rotating heads each with a 215× 230 mm^2 detector. The crystal thickness is 6.35 mm and the material NaI(Tl) covers 33 PMTs per detector and has an intrinsic resolution of 3.5 mm for ^{99m}Tc [50] and an energy resolution of 9.5 %. These detectors feature multiplexed multipinhole collimation with 9 up to 16 (optional) pinholes per detector. In this study, we used the 0.6-mm and 1-mm pinhole collimators. More information can be found in in the literature [50–53], and a selection of user applications with the NanoSPECT-NSO have also been described [54, 55].

Evaluation strategy

The highest achievable resolutions with the systems were measured with ^{99m}Tc using the HR collimators and by scanning both a phantom with three hot rod inserts (Fig. 4a) as well as a line source. In addition, to mimic GP use (higher throughput because of the higher sensitivity but with reduced resolution) of the systems, the GP collimators were used to measure spatial resolution, sensitivity, uniformity and contrast recovery. A matched pinhole diameter of 1 mm for the GP collimators was used for all three systems in this study.

HR mode measurements

The collimators used were the respective vendors' highest resolution option, being 0.35-mm ultrahigh resolution (UHR) WB/focused mouse (75 pinholes) for the U-SPECT-II, the 0.5-mm low-energy (LE) mouse (5 pinholes/plate) for the X-SPECT, and the 0.6-mm UHR/focused mouse (9 pinholes/plate) for NanoSPECT-NSO (Table 1).

To obtain a qualitative measure of the resolution over the entire transaxial FOV, we scanned a mouse-sized phantom containing three hot rod inserts (outer diameter of one insert 1 cm, length 0.85 cm) with capillary diameters ranging from 0.35 mm to 0.75 mm (Fig. 4a, Table 2) for 1 h on all systems. The minimum distance between the capillaries in the phantom within a certain segment was equal to the capillary diameter in that segment. These mouse hot rod phantoms were filled with a ^{99m}Tc solution at a concentration of 500 MBq/ml to avoid noise as a confounding factor in this HR experiment. Circular scans were performed for the X-SPECT (all the scans in the study were circular with the X-SPECT) and the NanoSPECT-NSO as the phantom fitted the FOV of one bed position. All the scans in the study for the X-SPECT had 64 detector positions and 24 detector positions for the NanoSPECT-NSO. Depending on the acceleration of the motor and the maximum speed of rotation, 64 detector positions result in about 30 s of dead time for the X-SPECT while 24 detector positions result in about 48 s of dead time for the NanoSPECT-NSO with an additional 1 s for changing the bed position. With the U-SPECT-II, 17 bed translations (3 min 32 s per position + 36 s total overhead due to bed travel and detector initialization) with overlapping FOVs were automatically performed.

Besides this qualitative evaluation of the reconstructed spatial resolution, we also measured the full-width at half-maximum (FWHM) of two line sources (polyethylene tubing filled with 370 MBq/ml ^{99m}Tc) with an inner diameter of 0.28 mm for 1 h with one line source (2.5 cm length) axially oriented and the other (1.5 cm length) transaxially positioned (Fig. 2). With the NanoSPECT-NSO, a spiral scan of three 'bed positions' was used. With the U-SPECT-II, 36 bed positions were needed with 1 min 40 s per position (+1 min 12 s). The FWHMs were determined from profiles taken over several reconstructed cross-sectional image slices, and these values were averaged to obtain one value, which was recorded as the FWHM (± SD). The axial and transaxial resolution was then defined, and the average of these two resolutions was also determined as (transaxial + axial)/2. SPECT integral and differential uniformities were measured for a region containing 75 % of the FOV (CFOV) of uniformly filled cylinders. The uniform phantom was a

Table 1 HR and GP collimators

System	HR		GP	
U-SPECT-II	Pinhole diameter (mm)	0.35	0.6	1
	No. of pinholes	75	75	75
	Name	UHR-Mouse	GP-mouse	UHS-mouse
X-SPECT	Pinhole diameter (mm)	0.5	1	
	No. of pinholes	20 (four heads)	20 (four heads)	
	Name	LE mouse	LE rat	
NanoSPECT-NSO	Pinhole diameter (mm)	0.6	1	
	No. of pinholes	36 (four heads)	36 (four heads)	
	Name	UHR/mouse focused (Apt 4)	HR/WB mouse standard (Apt 3)	

20-ml syringe (internal diameter 19 mm) filled with 8 ml ^{99m}Tc solution (78 MBq) and was scanned for 2 h. With the NanoSPECT-NSO, a spiral scan of two 'bed positions' was used. With the U-SPECT-II, 54 positions (2 min 15 s per position + total overhead of 1 min 35 s) were needed. With the NanoSPECT-NSO, a 5-ml syringe (internal diameter 12 mm) was also additionally scanned because with the 20-ml syringe scan severe artifacts were observed in the NanoSPECT-NSO images. Integral and differential uniformities were then calculated using the NEMA (National Electrical Manufacturers Association) formula [56]:

$$\text{Uniformity}\,(\%) = 100 \times \frac{\text{Max count} - \text{Min count}}{\text{Max count} + \text{Min count}} \qquad (1)$$

The integral uniformity indicates the uniformity calculated over the CFOV, whereas the differential uniformity is calculated for all sets of three contiguous pixels separately. The maximum over these sets is then recorded as the differential uniformity [57]. Uniformity measures are strongly affected by the voxel size and image resolution. In order to prevent differences in uniformity between the various systems solely due to the resolution effect, the images were smoothed with a gaussian filter complementing the resolution of each scanner. The gaussian filter kernel widths to result in an equal resolution of 1 mm were 0.92, 0.66 and 0.80 mm FWHM for the U-SPECT-II, the X-SPECT and the NanoSPECT-NSO, respectively.

The average object-to-collimator distance for the U-SPECT-II was 22 mm while the ROR for both the X-SPECT and the NanoSPECT-NSO was 30 mm. However, to encompass the phantom with the three hot rod inserts a ROR of 35 mm was also needed for the X-SPECT. These RORs were the closest possible to each system's hardware and software.

Ordered subset expectation maximization (OSEM) image reconstruction was used for all systems and also the more specific POSEM (pixel-based subsets [58], [29]) for the U-SPECT-II. For the NanoSPECT-NSO the raw projections were smoothed first (1.25 mm gaussian kernel) to suppress the noise prior to reconstruction. The software-recommended settings were used for the number of iterations and subsets (nine iterations with 16 subsets per iteration for U-SPECT-II, five iterations with 8 subsets per iteration for X-SPECT, and three iterations with 8 subsets per iteration for NanoSPECT-NSO) with the lowest image voxel sizes possible (0.125, 0.25 and 0.13 mm, respectively). An energy window of 20 % was set around 140 keV for all three systems.

GP mode measurements

For the evaluation of the GP mode, collimators with a 1-mm pinhole size were used for all systems; i.e. the 75-multipinhole tube for the MILabs U-SPECT-II, and a 5- and 9-multipinhole plate per head for the X-SPECT and the NanoSPECT-NSO, respectively (Table 1). Note that our definition of GP collimator (i.e. 1-mm pinhole diameter) does not correspond to the names the different vendors use to market their collimators. Therefore, we also included the U-SPECT-II measurements with the 0.6-mm pinhole collimator aperture in the GP mode data. Hence, the collimator of choice for imaging the mouse-sized phantoms in GP mode was also based on the

Table 2 The dimensions of the hot rod capillaries and scan durations used for the different isotopes at the same concentration

Isotope	HR collimator (mm)	GP 1-mm collimator (mm)	GP U-SPECT-II 0.6-mm collimator (mm)	Scan time (h)
^{99m}Tc	0.35, 0.4, 0.45, 0.5, 0.6, 0.75	0.7, 0.8, 0.9, 1.0, 1.2, 1.5	0.35, 0.4, 0.45, 0.5, 0.6, 0.75	1
^{111}In	–	0.7, 0.8, 0.9, 1.0, 1.2, 1.5	0.35, 0.4, 0.45, 0.5, 0.6, 0.75	0.949
^{125}I	–	0.7, 0.8, 0.9, 1.0, 1.2, 1.5	0.25, 0.3, 0.35, 0.4, 0.5, 0.6	0.944

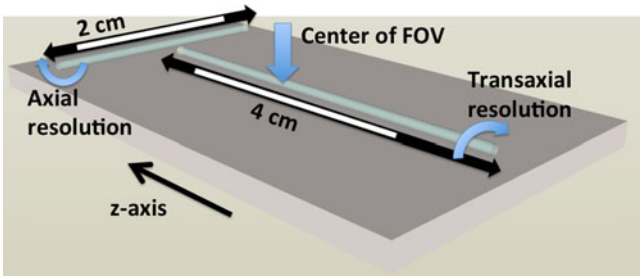

Fig. 2 Schematic drawing of the line sources, their positioning and dimensions. The *black double-headed arrows* show the length of the capillaries. The *white part* in the black arrows indicates the part used to extract the profiles

manufacturers' recommendations. The resolution with these collimators was measured again for 1 h using the two line sources discussed in the previous section and a hot rod phantom with capillary diameters in the range 0.7 mm to 1.5 mm (Table 2) and filled with a ^{99m}Tc solution at a concentration of 500 MBq/ml. We used an additional hot rod resolution phantom with smaller capillaries (0.35 to 0.75 mm) for the GP U-SPECT-II 0.6-mm collimator as this setup was able to achieve a higher resolution.

With the NanoSPECT-NSO, a spiral scan with three 'bed positions' and a circular scan were used for the line sources and the hot rod phantom, respectively. With the U-SPECT-II, 12 positions (5 min per position + total overhead of 24 s) and 18 positions (3 min 20 s per position + total overhead of 24 s) were needed for the line sources and the hot rod phantom, respectively. Sensitivity (in counts per second per megabecquerel) was measured using a ^{99m}Tc point source with known activity (2.96 MBq) positioned in the centre of the FOV and scanned for 1 h. SPECT integral and differential uniformities were measured as described for the HR mode measurements with a syringe of the same size (20 ml). With the NanoSPECT-NSO, a spiral scan of four 'bed positions' was used. With the U-SPECT-II, 72 positions (1 min 40 s per position + total overhead time of 2 min 24 s) were needed. We again matched the resolution as for the HR mode uniformity measurements with a gaussian filter kernel of 0.98, 0.8 and 0.9 mm FWHM for the U-SPECT-II, the X-SPECT and the NanoSPECT-NSO, respectively, resulting in a common resolution of 1.2 mm.

To measure contrast recovery, we designed and measured a mouse-sized phantom with five capillaries (Table 3 and Fig. 3) for 20 min. A spiral scan of three 'bed positions' was used with the NanoSPECT-NSO. To measure the mouse-sized phantom with the U-SPECT-II system, a total of 63 bed positions, 19 s for each position (+ 2 min 6 s total overhead) were needed. The background (5 MBq/ml) and the four smallest capillaries (20 MBq/ml) were filled with a ^{99m}Tc solution to result in a capillary-to-background ratio of 4 to 1. The 2-mm capillary was left unfilled to create a cold

Table 3 Dimensions of the capillary phantom. Units are millimetres except volume in millilitres

Phantom component	Dimension	Value
Outer phantom	Length	50
	Diameter	20
Rings	Length	10
	Diameter	18
	Radius of inner hole	2
Capillaries	Overall length	40
	Length in hot background	20
	Radius from centre	5
Capillary 1	Inner diameter	2
	Wall thickness	0.4
Capillary 2	Inner diameter	1.5
	Wall thickness	0.3
Capillary 3	Inner diameter	1
	Wall thickness	0.2
Capillary 4	Inner diameter	0.8
	Wall thickness	0.2
Capillary 5	Inner diameter	0.6
	Wall thickness	0.24
Background volume		9.5

region in a hot background. Capillary and background volumes of interest (VOIs) were delineated on the corresponding CT images. The VOIs were repeated in seven 1-mm thick transaxial slices 1.5 mm apart to obtain seven

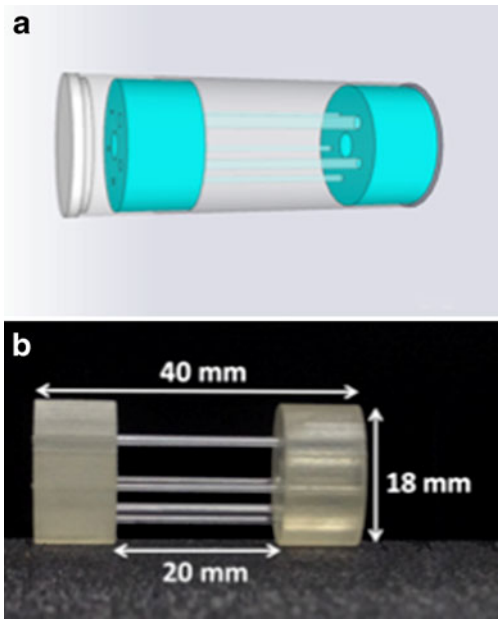

Fig. 3 **a** Drawing of the contrast phantom with five capillaries inside surrounded by a hot background. **b** Photograph of the capillaries and the rings. For dimensions, see Table 3

results. The contrast recovery coefficient (CRC_{hot}) was then calculated as follows:

$$CRC_{hot} = \frac{\frac{m_{hot} - m_{BG}}{m_{BG}}}{C_{true} - 1} \quad (2)$$

where m_{hot} and m_{BG} are the mean concentrations measured in capillary and background VOIs averaged over the seven results and C_{true} is the real capillary-to-background ratio.

The cold-to-background ratio (CBR_{air}) was defined as the activity measured in the cold region (m_{cold}) divided by the mean of the background concentration (m_{BG}), which we represent as CRC_{cold}:

$$\begin{aligned} CBR_{air} &= \frac{m_{cold}}{m_{BG}} \\ CRC_{cold} &= 1 - CBR_{air} \end{aligned} \quad (3)$$

The images were repeatedly smoothed with a 0.3-mm gaussian filter to obtain the contrast recovery at different levels of background standard deviation. This noise coefficient (NC) was calculated as follows [59]:

$$NC(\%) = 100 \times \frac{1}{P} \sum_{p}^{p} \frac{\sigma_p}{m_p} \quad (4)$$

where P is the total number of pixels in the background VOI and for each background pixel p, σ_p is the standard deviation and m_p the mean calculated from the seven slices. The average object-to-collimator distance in these GP measurements for the U-SPECT-II was 22 mm while the RORs for the X-SPECT and the NanoSPECT were 35 mm and 30 mm, respectively. However, for the uniform cylinder a ROR of 45 mm was needed with the X-SPECT. The same number of iterations and subsets were used as in the HR measurements, and the software selected voxel sizes for the 1-mm collimators for the U-SPECT-II, X-SPECT and NanoSPECT-NSO were 0.2, 0.5 and 0.2 mm, respectively.

Other isotopes Besides ^{99m}Tc, we also use ^{111}In and ^{125}I in our experiments. Different scan times were set to have the same number of decays (Table 2). For these extra isotopes we measured GP spatial resolution (line source and hot rod phantom) and uniformity as described in the previous paragraph. As with ^{99m}Tc, OSEM reconstruction was applied with a 20 % energy window set around the main peaks for ^{111}In and a 100 % window around the 27 keV peak for ^{125}I.

Results

System measurements

Spatial resolution – HR collimators

Figure 4 shows the mouse-sized phantom with the three hot rod inserts measured with the HR apertures and shows qualitatively the spatial resolution in the entire FOV. The U-SPECT-II was able to resolve rods as small as 0.4 mm (Fig. 4b), the X-SPECT (Fig. 4c) was able to resolve rods of 0.75 mm, and the NanoSPECT-NSO was able to resolve rods as small as 0.6 mm, although with the NanoSPECT-NSO the transaxial FOV was only 20 mm leaving one hot rod phantom truncated (Fig. 4d). The resolutions with the line sources in the centre of the FOV (Table 4) and with these HR apertures (average of axial and transaxial) were as small as 0.38 mm with the U-SPECT-II, 0.49 mm with the X-SPECT and 0.66 mm with the NanoSPECT-NSO.

Spatial resolution – GP collimators

Figure 5 shows the hot rod phantoms measured with the U-SPECT-II 0.6-mm apertures and with the 1-mm apertures of all the scanners. The U-SPECT-II 0.6-mm collimator resolved rods of 0.45 mm with ^{99m}Tc and between 0.5 and 0.6 mm with ^{111}In and ^{125}I. The FWHM of the line sources acquired with this collimator (Table 4) gave a quantitative result for the spatial resolution. The average resolutions were 0.63, 0.71 and 0.66 mm for ^{99m}Tc, ^{111}In and ^{125}I, respectively. For the 1-mm collimators and ^{99m}Tc, the U-SPECT-II resolved rods as small as 0.7 mm, the X-SPECT resolved rods of 0.9 mm, and the NanoSPECT-NSO resolved rods of 0.8 mm. The average resolutions for the ^{99m}Tc line sources were 0.76 mm for the U-SPECT-II, 0.58 mm for the X-SPECT, and 0.69 mm for the NanoSPECT-NSO. For ^{111}In, the U-SPECT-II resolved rods of 0.7 to 0.8, and the X-SPECT and the NanoSPECT-NSO resolved rods of 0.9 to 1 mm. The average resolutions of the ^{111}In line sources for the U-SPECT-II were 0.85 mm, for the X-SPECT 0.80 mm, and for the NanoSPECT-NSO 0.78 mm. For ^{125}I, the U-SPECT-II resolved rods from 0.8 to 0.9 mm, and the X-SPECT and the NanoSPECT-NSO resolved rods of 0.9 mm. The average resolutions of the line sources for the U-SPECT-II were 0.79 mm, for the X-SPECT 0.68 mm, and for the NanoSPECT-NSO 0.92 mm.

Sensitivity

The point source sensitivities measured with ^{99m}Tc and the 1-mm pinhole apertures for the U-SPECT-II was 3,984 cps/MBq or 0.39 % and 1,500 cps/MBq or 0.15 % for the 0.6-mm collimator, for the X-SPECT 620 cps/MBq or 0.06 % (= 4×155 cps/MBq of the one-head system), and for the NanoSPECT 751 cps/MBq or 0.07 %.

Uniformity

The HR/GP integral and differential uniformities are summarized in Table 5. The HR integral and differential uniformities measured with ^{99m}Tc were 31 %/15 % for the U-

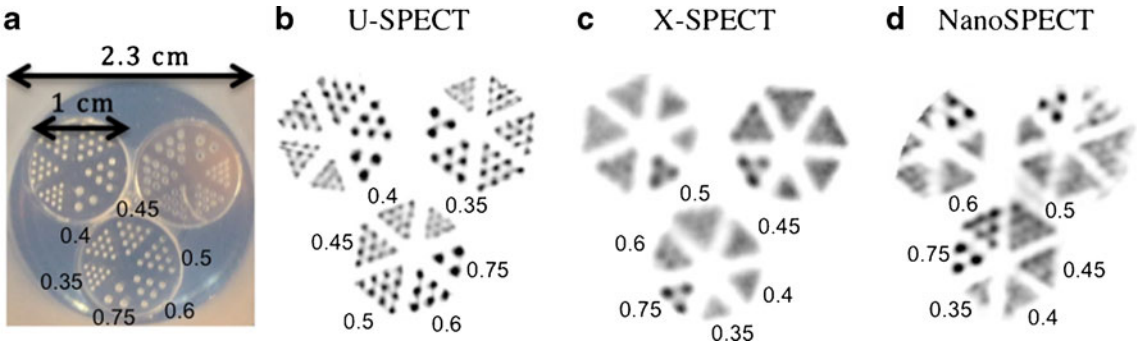

Fig. 4 Mouse-sized phantom with three hot rod inserts (capillaries 0.35, 0.4, 0.45, 0.5, 0.6 and 0.75 mm) measured with the three systems using their HR collimators: **a** the phantom, **b** U-SPECT-II 0.35-mm collimator, **c** X-SPECT 0.5-mm collimator, and **d** NanoSPECT-NSO 0.6-mm collimator

SPECT-II, 56 %/38 % for the X-SPECT and 93 %/64 % for the NanoSPECT-NSO. Since the 20-ml syringe with the NanoSPECT-NSO produced severe artifacts, a 5-ml syringe was also scanned and resulted in better uniformities of 33 %/21 %. The GP ^{99m}Tc uniformities were similar to the HR values. The GP uniformity measured with the higher energy isotope ^{111}In was only slightly different while the uniformity values with ^{125}I were even worse (Table 5).

Contrast recovery and cold-to-background ratio

Figure 6 shows the CRC_{hot} and CRC_{cold} curves for the different capillary diameters and scanners as a function of the standard deviation of the background. At a noise level of 8 %, the U-SPECT-II achieved a CRC ranging from 0.05 for the 0.6-mm rod to 0.42 for the 1.5-mm rod. For this largest rod, the U-SPECT-II achieved a CRC of 0.34 at a noise level of 5 % and 0.45 at a noise level of 10 %. At this latter noise level the CRC_{cold} was 0.70 for the U-SPECT-II. At a noise level of 8 %, the X-SPECT achieved a CRC ranging from 0.07 for the 0.6-mm rod to 0.37 for the 1.5-mm rod. For this largest rod, the X-SPECT achieved a CRC of 0.26 at a noise level of 5 % and 0.42 at a noise level of 10 %. The CRC_{cold} at the 10 % noise level was 0.52. Finally, at a noise level of 8 %, the NanoSPECT-NSO achieved a CRC ranging from 0.09 for the 0.6-mm rod to 0.34 for the 1.5-mm rod. For this 1.5 mm rod, the NanoSPECT-NSO achieved a CRC of 0.27 at a noise level of 5 % and 0.36 at a noise level of 10 %. At this 10 % noise level, the CRC_{cold} was 0.42 for the NanoSPECT-NSO. Cross-sections of the phantom are shown in Fig. 7 at a noise level of 10 %.

Discussion

The performance of three state-of-the-art multipinhole μSPECT systems, all configured for mouse imaging, was

Table 4 Spatial resolutions: line sources

Isotope	Scanner	Collimator	ROR (mm)	Resolution (mm)		
				Transaxial	Axial	Average
^{99m}Tc	U-SPECT-II	HR	22[a]	0.37±0.06	0.39±0.06	0.38
	X-SPECT	HR	30	0.45±0.09	0.53±0.11	0.49
	NanoSPECT-NSO	HR	30	0.48±0.05	0.83±0.07	0.66
	U-SPECT-II	GP 1 mm	22[a]	0.76±0.03	0.76±0.04	0.76
	U-SPECT-II	GP 0.6 mm	22[a]	0.61±0.02	0.65±0.01	0.63
	X-SPECT	GP	30	0.53±0.10	0.62±0.07	0.58
	NanoSPECT-NSO	GP	30	0.56±0.06	0.82±0.12	0.69
^{111}In	U-SPECT-II	GP 1 mm	22[a]	0.84±0.05	0.86±0.02	0.85
	U-SPECT-II	GP 0.6 mm	22[a]	0.71±0.03	0.70±0.03	0.71
	X-SPECT	GP	30	0.77±0.04	0.82±0.07	0.80
	NanoSPECT-NSO	GP	30	0.67±0.08	0.89±0.12	0.78
^{125}I	U-SPECT-II	GP 1 mm	22[a]	0.80±0.06	0.78±0.08	0.79
	U-SPECT-II	GP 0.6 mm	22[a]	0.65±0.07	0.67±0.06	0.66
	X-SPECT	GP	30	0.69±0.1	0.67±0.07	0.68
	NanoSPECT-NSO	GP	30	0.85±0.08	0.98±0.06	0.92

[a]Average object to collimator tube distance

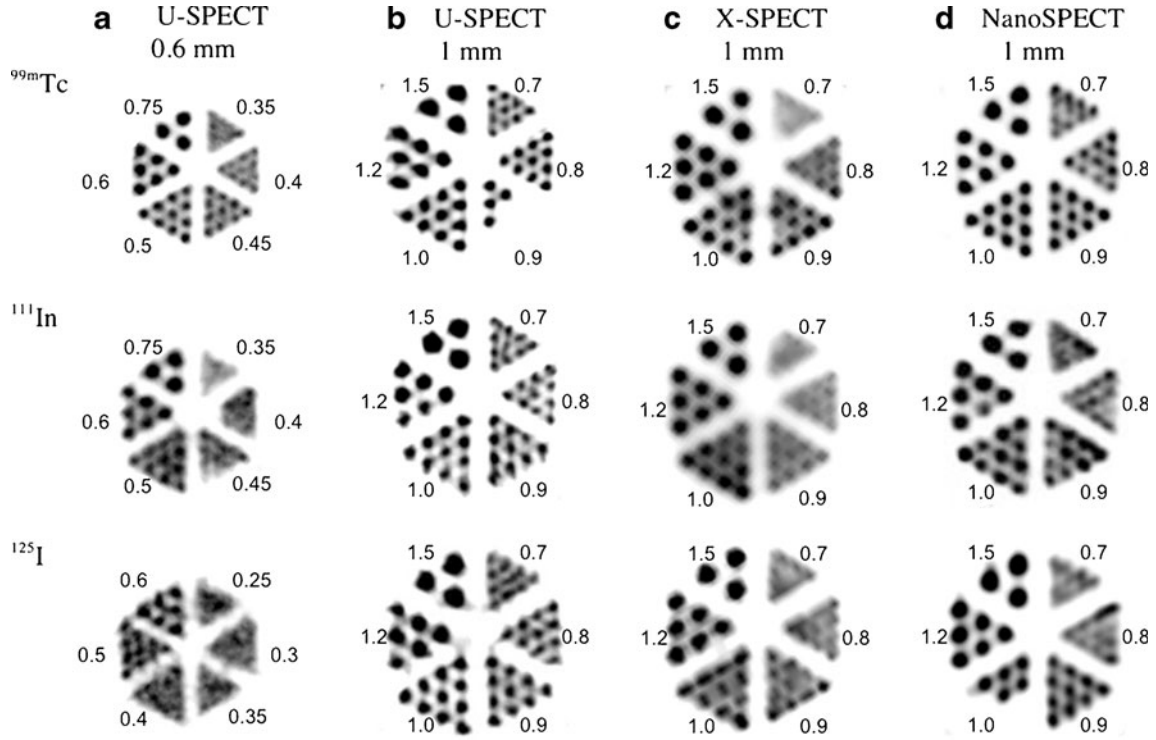

Fig. 5 **a** GP scans of the hot rod phantom with 0.35, 0.4, 0.45, 0.5, 0.6, 0.75-mm capillaries with the 0.6-mm pinhole collimator of the U-SPECT-II (for ^{125}I the hot rod phantom with 0.25, 0.3, 0.35, 0.4, 0.5, 0.6-mm capillaries was scanned). **b–d** GP scans of the hot rod phantom with 0.7, 0.8, 0.9, 1.0, 1.2, 1.5-mm capillaries with the 1-mm pinhole collimator of the U-SPECT-II, X-SPECT and NanoSPECT-NSO, respectively (500 MBq/ml, scan time 1 h)

evaluated. Although each system has been evaluated previously [37, 47, 51–53], there was no comparative study testing the systems with the same set of standardized experiments. We report here on the performance metrics for the objective characterization of these widely used μSPECT systems. We kept all acquisition parameters for all measurements as equal as possible between the scanners. The reconstruction parameters were chosen each time based on the recommended parameters of the software and the vendors' experience with the systems.

Besides measuring the basic characteristics of these systems, the size of the FOV (and information on spiral pitch and number of bed positions needed) is an equally important aspect when using these μSPECT systems for molecular

Table 5 GP integral and differential uniformities for the HR and GP collimators (a lower number represents better uniformity)

Isotope	Scanner	Collimator	ROR (mm)	Integral uniformity (%)	Differential uniformity (%)
^{99m}Tc	U-SPECT-II	HR	22[b]	31	15
	X-SPECT	HR	30	56	38
	NanoSPECT-NSO	HR	30	93	64
	NanoSPECT-NSO	HR	30	33[a]	21[a]
	U-SPECT-II	GP	22[b]	30	14
	X-SPECT	GP	30	50	30
	NanoSPECT-NSO	GP	30	38	25
^{111}In	U-SPECT-II	GP	22[b]	34	15
	X-SPECT	GP	30	52	28
	NanoSPECT-NSO	GP	30	35	24
^{125}I	U-SPECT-II	GP	22[b]	41	26
	X-SPECT	GP	30	65	36
	NanoSPECT-NSO	GP	30	44	35

[a]HR values from the NanoSPECT-NSO measured with a 5-ml syringe

[b]Average object to collimator tube distance

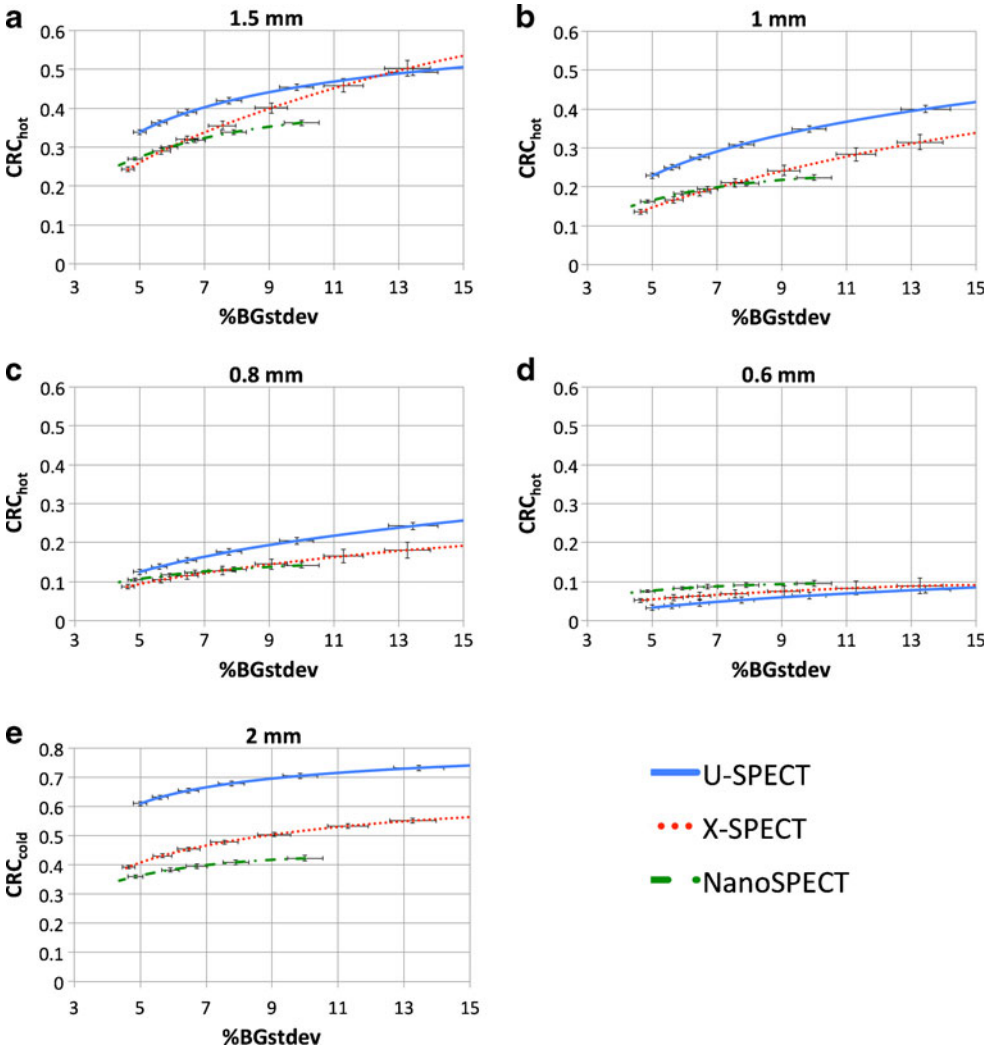

Fig. 6 **a–d** CRC_{hot} curves for the different capillary diameters as a function of the standard deviation of the background. **e** CRC_{cold} curves for the 2-mm cold capillary (only air) as a function of the standard deviation of the background

imaging in daily preclinical routine. These parameters will determine the injected dose and scan time, and may put the sensitivity versus resolution trade-off in another light. As discussed by Harteveld et al. in 2011 [60], a standard for μSPECT is still lacking, and they evaluated a μSPECT scanner (U-SPECT-II) using the NEMA NU 4 μPET phantom. This NEMA NU4 μPET IQ phantom has several disadvantages when used to evaluate μSPECT systems: (1) the diameters of the hot rods range from 1 to 5 mm which is above the current state-of-the-art μSPECT achievable submillimetre resolution, (2) the 30-mm diameter of the phantom does not allow μSPECT multipinhole scanners to be used in HR mode (small ROR and high magnification), and (3) the phantom does not offer the possibility of having hot rods on a warm background. To address some of these issues, Visser et al. [61] developed an alternative phantom dedicated to image quality evaluation with μSPECT having a smaller outer diameter of 23.45 mm and hot rods down to 0.35 mm diameter which is ideally suited to current μSPECT systems. These authors considered that having hot rods in a warm background would be more realistic. Their cold background configuration was based on the physical limitations that prevent the production of hot spheres with physical walls smaller than the spatial resolution [62]. As a solution to this limitation we constructed a μSPECT IQ phantom using ultrathin round borosilicate capillaries (internal diameter 0.6, 0.8, 1, 1.5 and 2 mm) aligned using two multijet-modelled (Shapeways, Eindhoven) rings (acrylic plastic, 1.8×1.8×1.0 cm). Our custom-made contrast phantom thus has a warm background and the capillary wall thickness ranged only between 0.2 mm for the smallest and 0.4 mm for the biggest capillary, which is smaller than half of the spatial resolution, measured with the 1-mm GP collimators (Table 4). An additional feature of our phantom is the longer capillaries (20 mm versus 6.5 mm in the IQ phantom) so that we can measure contrast/resolution over more slices and with a more realistic FOV size. This serves also as an indirect measure for the sensitivity over a larger FOV with many bed positions needed for the U-SPECT-II. Also the capillary

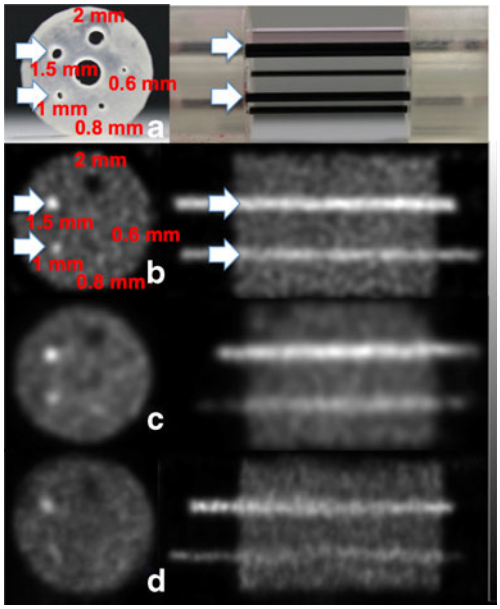

Fig. 7 **a** Photograph of the phantom. The *white arrows* indicate the 1.5-mm and 1-mm capillaries. The capillaries are filled with a red colouring liquid for visualization, except for the 2-mm capillary. **b–d** Transverse and sagittal cross-sections of the contrast phantom with 10 % background standard deviation measured with (**b**) the U-SPECT-II, (**c**) the X-SPECT and (**d**) the NanoSPECT-NSO

diameters are optimized to evaluate the different scanners equipped with high-sensitivity 1-mm collimators for mice (rods ranging from 0.6 to 2.0 mm). This phantom may also be used to characterize different collimators and acquisition and reconstruction parameters, and the effect of scatter and attenuation correction.

When all systems were equipped with their HR collimators, the U-SPECT-II obtained the highest spatial resolution over the entire FOV for the multi-hot rod phantom as well as for the line sources. This can be attributed to the smaller diameter of the pinholes and a larger number of pinholes, the higher pinhole magnification factor and the fact that the pinholes are on average closer to the object. This larger multi-hot rod phantom was truncated with the NanoSPECT-NSO due to the smaller transaxial FOV of the 0.6-mm collimators of this system. When using the GP collimators (1-mm aperture, and also the 0.6-mm aperture for the U-SPECT-II) to increase the sensitivity, the highest overall resolution was also obtained with the U-SPECT-II based on the assessment of a hot rod phantom (0.7, 0.8, 0.9, 1.0, 1.2, 1.5 mm) placed in the centre of the FOV. This was the case for all isotopes imaged. Due to the higher energy of the ^{111}In-emitted photons, the reconstructed resolution using this isotope was lower than for ^{99m}Tc as a result of increasing collimator scatter and penetration which was observed for all three systems tested. Similarly, the low energy of ^{125}I resulted in more object scatter and poorer detector resolution. However, for all three systems tested, the image quality obtained remained high, even with these more challenging isotopes.

When additionally evaluating the spatial resolution with the line source measurements for these GP collimators, the X-SPECT and NanoSPECT-NSO provided a higher reconstructed resolution, which contradicted the apparent resolution of the hot rod phantom images. The use of the crossed capillaries for resolution measurements has often been debated when iterative reconstruction with resolution recovery is used [63–65]. A possible explanation is, as discussed by Mok et al. [32], that the sensitivity gained from multiplexing may result in a better resolution for sparse objects such as the line sources. When larger, nonsparse, objects such as the hot rod and the uniformity are scanned such resolution gains are lost due to the increased amount of overlap in the projections [32, 66]. The axial resolution of the NanoSPECT-NSO was inferior to its transaxial FWHM. A possible explanation could be that the pitch of the spiral SPECT acquisition mode slightly deteriorates the axial resolution or that the overall resolution is degraded more at the edge of the FOV for the NanoSPECT-NSO. Such an off-centre resolution degradation can also be seen in Fig. 4d: in the centre of the FOV rods as small as 0.6 mm are resolved while at the edge only the 0.75-mm rods are resolved.

Point source sensitivity was measured for all systems with the 1-mm collimators resulting in the highest sensitivity for the U-SPECT-II. This was mainly due to more (75) pinholes, and their strong focus to the same area in the FOV. As a result of this arrangement a smaller FOV was covered in one bed position and this point source measurement with the U-SPECT-II only needed a single position. The lower sensitivity of the X-SPECT (5 pinholes) and the NanoSPECT (9 pinholes) can be explained as these systems have fewer pinholes and also the NanoSPECT-NSO pinholes do not focus on the same area in the FOV, and therefore span a larger FOV. In addition, when measuring a point source, the X-SPECT and the NanoSPECT-NSO do not benefit, in terms of sensitivity, from their multiplexing capabilities as the point source projections do not overlap. To resolve the difficulties in comparing and interpreting point source sensitivity values of the different systems as a result of the diverse approaches (strong focusing pinholes, multiplexing, different FOV) amongst them, a CRC study was performed. Alternatively volume sensitivity could be considered for which the sensitivity of the NanoSPECT-NSO and the X-SPECT systems would benefit from multiplexing. However as less spatial information is available for photons when projections overlap the gain sensitivity gain is in a sense artificial. In addition, the sensitivity gained from multiplexing will depend on the activity distribution [32].

As can be concluded from Fig. 6, the U-SPECT-II maintains its higher sensitivity and resolution for a full-size FOV when acquiring this contrast recovery μSPECT image

quality phantom, especially for the 1.5-mm and the 1.0 mm capillaries. For the 0.8-mm hot rods the performance of the U-SPECT-II and the NanoSPECT-NSO were comparable and the 0.6-mm capillaries were not resolved by any of the three systems when using the GP 1-mm collimator. In terms of the CRC_{cold}, the U-SPECT-II clearly achieved better performance than the other two systems. The better CRC_{hot} and CRC_{cold} values for the U-SPECT-II may be attributed to the lack of multiplexing and/or higher resolution obtainable over the entire phantom with the scanning focusing method [35].

The U-SPECT-II provided the best uniformity values (in both HR and GP mode). The X-SPECT values were higher (i.e. less uniform) but not significantly so than the U-SPECT-II values (Mann-Whitney test, p=0.148). No artifacts were seen in the uniformity images (Fig. 8) for the U-SPECT-II or the X-SPECT. On the contrary, severe artifacts were seen on the NanoSPECT-NSO HR uniformity images which were probably a consequence of too much multiplexing (i.e. true overlap) [33] making the syringe look smaller (Fig. 8) with patterns inside. Replacing the 20-ml syringe with a 5-ml syringe resulted in normalization of the NanoSPECT-NSO HR image uniformity values (Table 5). In many small-animal imaging studies some of the activity is usually clustered in small volumes, which may render these artifacts less severe but may still result in erroneous quantification.

To make the performance comparison between the μSPECT scanners more complete we also refer to the results obtained by Magota et al. [67] and Boisson et al. [68] with the Inveon (dual head) SPECT system. In contrast to our study involving multipinhole collimators, Magota et al. performed an evaluation with a single-pinhole collimator. The ^{99m}Tc spatial resolution was measured with an ultramicro hot spot phantom (0.75, 1.00, 1.35, 1.7, 2.00 and 2.4 mm; Data Spectrum Corporation) filled with a concentration of 15.9 MBq/ml for 32 min. The phantom resolutions obtained with the 0.5-mm and 1-mm pinhole collimators (ROR 25 mm) were 0.84 mm and 1.20 mm, respectively. Boisson et al. obtained a spatial resolution of 1.0 mm by measuring line sources with the 1-mm multipinhole (five pinholes, mouse WB) collimators rotating at 30 mm ROR. Both studies showed resolutions (both in HR and GP mode) that were inferior to the obtained resolutions in this study. A cylindrical phantom (internal diameter 2.5 cm, length 9 cm) filled with 117 MBq of ^{99m}Tc (2.6 MBq/ml) was scanned by Magota et al. for 48 min with a ROR of 25 mm to obtain both volume sensitivity and integral uniformity. The sensitivity was 76 cps/MBq and the integral uniformity was 37 %. Sensitivity was evidently low for this single-pinhole system. The integral uniformity was comparable to that obtained with the scanners in our study. Boisson et al. obtained a system sensitivity of 403.6 cps/MBq with the 1-mm mouse WB collimators which is inferior to the values obtained in our study with the other three systems. One has to bear in mind that Magota et al. and Boisson et al. obtained their results with a different set of phantoms rendering direct comparison difficult.

Besides the system hardware, imaging performance also depends on maintenance, quality control, calibrations and environment (e.g. temperature). The CZT detectors in the X-SPECT, for example, may be prone to minute impurities associated with LE spectral tailing, pixel dropouts, hot spots and nonuniform response. Mechanical calibration is mandatory for rotating systems (X-SPECT and NanoSPECT-NSO) to accurately define the geometry of a detector rotating in a

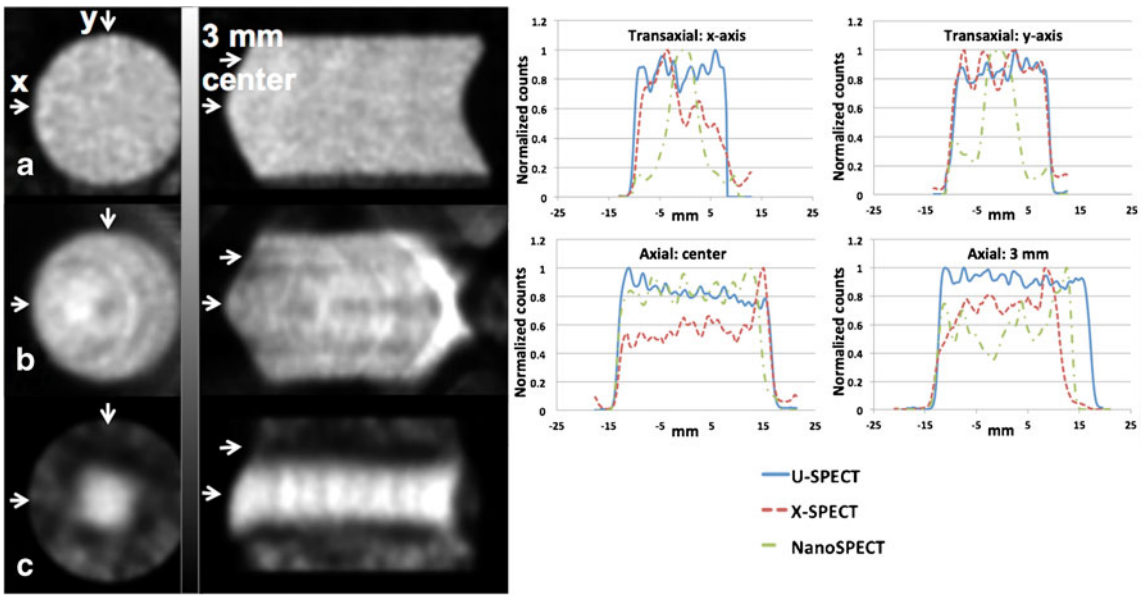

Fig. 8 Transaxial and axial HR uniformity images measured with (**a**) the U-SPECT-II (**b**) the X-SPECT and (**c**) the NanoSPECT-NSO. Transaxial profiles (x and y directions through the centre) and axial profiles (in the centre and 3 mm from the syringe edge) are shown

circular orbit. The more the system is reconfigured for different tasks (changing collimators, altering ROR), the more frequently will recalibration be required.

Future work will include comparisons using collimators designed for imaging rat-sized objects and in vivo experiments to complement our phantom-based findings. Also, the NEMA has now assembled a task force that has started designing a standard phantom for image quality evaluations in μSPECT.

All three scanners have made a large progress compared to the early human SPECTcameras that were modified for small animal imaging by using pinhole collimatorplates [8–10, 12, 13, 69] and evolve continuously through hardware upgrades such as the VECTor for Milabs and the NanoSPECT-Plus or NanoSPECT-II for Bioscan. The μSPECT system of choice depends on the applications for which it is used, the need for performance or the values placed on flexibility and cost.

Conclusion

We compared three state-of-the-art μSPECT systems based on image quality parameters including spatial resolution, reconstructed image uniformity, point source sensitivity and contrast recovery. To evaluate contrast recovery we designed and built a contrast-to-noise phantom which, to the best of our knowledge for the first time, provided the ability to measure hot contrast on a warm background in the submillimetre resolution range. We believe our evaluation realistically reflected the potential of each system to acquire mouse-sized objects.

Acknowledgments This work was supported by the University of Antwerp, the Research Foundation – Flanders (FWO), the Belgian Science Policy Office (BELSPO), iMinds and Ghent University. The authors would like to thank Peter Laverman of Radboud University Nijmegen, Ruud Ramakers of the University Medical Center Utrecht, Ciara Finucane and Jerome Burnet of Queen Mary, University of London, and Alessandro Passeri of the University of Florence for their cooperation and technical assistance with, respectively, the U-SPECT-II, the NanoSPECT-NSO and the X-SPECT measurements.

Conflicts of interest None.

References

1. Mankoff DA. A definition of molecular imaging. J Nucl Med. 2007;48:18N, 21N.
2. Cherry SR. In vivo molecular and genomic imaging: new challenges for imaging physics. Phys Med Biol. 2004;49:R13–48.
3. Bailey DL, Karp JS, Surti S. Physics and instrumentation in PET, in positron emission tomography: basic science and clinical practice. Philadelphia: Springer; 2003. p. 41–67.
4. Ishizu K, Mukai T, Yonekura Y, Pagani M, Fujita T, Magata Y, et al. Ultra-high resolution SPECT system using four pinhole collimators for small animal studies. J Nucl Med. 1995;36:2282–7.
5. Jaszczak RJ, Li J, Wang H, Zalutsky MR, Coleman RE. Pinhole collimation for ultra-high-resolution, small-field-of-view SPECT. Phys Med Biol. 1994;39:425–37.
6. McElroy DP, MacDonald LR, Beekman FJ, Yuchuan Wang, Patt BE, Iwanczyk JS, et al. Evaluation of A-SPECT: a desktop pinhole SPECT system for small animal imaging. Nuclear Science Symposium Conference Record, 2001 IEEE, vol. 3, pp. 1835–1839, 2001. doi:10.1109/NSSMIC.2001.1008699.
7. Weber DA, Ivanovic M, Franceschi D, Strand SE, Erlandsson K, Franceschi M, et al. Pinhole SPECT: an approach to in vivo high resolution SPECT imaging in small laboratory animals. J Nucl Med. 1994;35:342–8.
8. Beekman FJ, Vastenhouw B. Design and simulation of a high-resolution stationary SPECT system for small animals. Phys Med Biol. 2004;49:4579–92.
9. Beekman FJ, van der Have F, Vastenhouw B, van der Linden AJA, van Rijk PP, Burbach JPH, et al. U-SPECT-I: a novel system for submillimeter-resolution tomography with radiolabeled molecules in mice. J Nucl Med. 2005;46:1194–200.
10. Wilson DW, Barrett HH, Furenlid LR. A new design for a SPECT small-animal imager. Nuclear Science Symposium Conference Record, 2001 IEEE, vol. 3, pp. 1826–1829, 2001.doi:10.1109/NSSMIC.2001.1008697.
11. Meikle SR, Kench P, Weisenberger AG, Wojcik R, Smith MF, Majewski S, et al. A prototype coded aperture detector for small animal SPECT. Nuclear Science Symposium Conference Record, 2001 IEEE, vol. 3, pp. 1580–1584, 2001.doi:10.1109/NSSMIC.2001.1008641.
12. Liu Z, Kastis GA, Stevenson GD, Barrett HH, Furenlid LR, Kupinski MA, et al. Quantitative analysis of acute myocardial infarct in rat hearts with ischemia-reperfusion using a high-resolution stationary SPECT system. J Nucl Med. 2002;43:933–9.
13. Rowe RK, Aarsvold JN, Barrett HH, Chen JC, Klein WP, Moore BA, et al. A stationary hemispherical SPECT imager for 3-dimensional brain imaging. J Nucl Med. 1993;34:474–80.
14. Schramm NU, Ebel G, Engeland U, Schurrat T, Behe M, Behr TM. High-resolution SPECT using multipinhole collimation. IEEE Trans Nucl Sci. 2003;50:315–20.
15. Lackas C, Schramm NU, Hoppin JW, Engeland U, Wirrwar A, Halling H. T-SPECT: a novel imaging technique for small animal research. IEEE Trans Nucl Sci. 2005;52:181–7.
16. Kim H, Furenlid LR, Crawford MJ, Wilson DW, Barber HB, Peterson TE, et al. SemiSPECT: a small-animal single-photon emission computed tomography (SPECT) imager based on eight cadmium zinc telluride (CZT) detector arrays. Med Phys. 2006;33:465–74.
17. Miller BW, Furenlid LR, Moore SK, Barber HB, Nagarkar VV, Barrett HH. System Integration of FastSPECT III, a Dedicated SPECT Rodent-Brain Imager Based on BazookaSPECT Detector Technology. IEEE Nucl Sci Symp Conf Rec (1997) 2009, Oct. 24 2009-Nov. 1 2009;4004–4008.
18. Beekman F, van der Have F. The pinhole: gateway to ultra-high-resolution three-dimensional radionuclide imaging. Eur J Nucl Med Mol Imaging. 2007;34:151–61.
19. Wu C, de Jong JR, van Andel HA G, van der Have F, Vastenhouw B, Laverman P, et al. Quantitative multi-pinhole small-animal SPECT: uniform versus non-uniform Chang attenuation correction. Phys Med Biol. 2011;56:N183–93.
20. Constantinesco A, Choquet P, Monassier L, Israel-Jost V, Mertz L. Assessment of left ventricular perfusion, volumes, and motion in mice using pinhole gated SPECT. J Nucl Med. 2005;46:1005–11.
21. Golestani R, Wu C, Tio RA, Zeebregts CJ, Petrov AD, Beekman FJ, et al. Small-animal SPECT and SPECT/CT: application in cardiovascular research. Eur J Nucl Med Mol Imaging. 2010;37:1766–77.
22. Auricchio A, Acton PD, Hildinger M, Louboutin JP, Plossl K, O'Connor E, et al. In vivo quantitative noninvasive imaging of

gene transfer by single-photon emission computerized tomography. Hum Gene Ther. 2003;14:255–61.
23. Kumar SR, Deutscher SL, Figueroa SD. Tumor targeting and SPECT imaging properties of an (111)In-labeled galectin-3 binding peptide in prostate carcinoma. Nucl Med Biol. 2009;36:137–46.
24. Gambini JP, Cabral P, Alonso O, Savio E, Figueroa SD, Zhang X, et al. Evaluation of 99mTc-glucarate as a breast cancer imaging agent in a xenograft animal model. Nucl Med Biol. 2011;38:255–60.
25. Luo SN, Wang Y, Lin JG, Qiu L, Cheng W, Zhai HZ, et al. Animal studies of (99m)Tc-i-PIDP: a new bone imaging agent. Appl Radiat Isotopes. 2011;69:1169–75.
26. Booij J, de Bruin K, de Win MML, Lavini C, den Heeten GJ, Habraken JBA. Imaging of striatal dopamine transporters in rat brain with single pinhole SPECT and co-aligned MRI is highly reproducible. Nucl Med Biol. 2003;30:643–9.
27. Bennink RJ, Hamann J, de Bruin K, ten Kate FJ, van Deventer SJ, te Velde AA. Dedicated pinhole SPECT of intestinal neutrophil recruitment in a mouse model of dextran sulfate sodium-induced colitis. J Nucl Med. 2005;46:526–31.
28. Goorden MC, Beekman FJ. High-resolution tomography of positron emitters with clustered pinhole SPECT. Phys Med Biol. 2010;55:1265–77.
29. van der Have F, Vastenhouw B, Rentmeester M, Beekman FJ. System calibration and statistical image reconstruction for ultra-high resolution stationary pinhole SPECT. IEEE Trans Med Imaging. 2008;27:960–71.
30. Miller BW, Van Holen R, Barrett H, Furenlid L. A system calibration and fast iterative reconstruction method for next-generation SPECT imagers. IEEE Trans Nucl Sci. 2012;59:1990–6.
31. Branderhorst W, Vastenhouw B, van der Have F, Blezer ELA, Bleeker WK, Beekman FJ. Targeted multi-pinhole SPECT. Eur J Nucl Med Mol Imaging. 2011;38:552–61.
32. Mok GS, Tsui BM, Beekman FJ. The effects of object activity distribution on multiplexing multi-pinhole SPECT. Phys Med Biol. 2011;56:2635–50.
33. Vunckx K, Suetens P, Nuyts J. Effect of overlapping projections on reconstruction image quality in multipinhole SPECT. IEEE Trans Med Imaging. 2008;27:972–83.
34. Cherry SR, Sorensen J, Phelps ME. Physics in nuclear medicine. Philadelphia: Saunders; 2012.
35. Vastenhouw B, Beekman F. Submillimeter total-body murine imaging with U-SPECT-I. J Nucl Med. 2007;48:487–93.
36. Vaissier PE, Goorden MC, Vastenhouw B, van der Have F, Ramakers RM, Beekman FJ. Fast spiral SPECT with stationary gamma-cameras and focusing pinholes. J Nucl Med. 2012;53:1292–9.
37. van der Have F, Vastenhouw B, Ramakers RM, Branderhorst W, Krah JO, Ji C, et al. U-SPECT-II: an ultra-high-resolution device for molecular small-animal imaging. J Nucl Med. 2009;50:599–605.
38. Wyckhuys T, Staelens S, Van Nieuwenhuyse B, Deleye S, Hallez H, Vonck K, et al. Hippocampal deep brain stimulation induces decreased rCBF in the hippocampal formation of the rat. Neuroimage. 2010;52:55–61.
39. Van Steenkiste C, Staelens S, Deleye S, De Vos F, Vandenberghe S, Geerts A, et al. Measurement of porto-systemic shunting in mice by novel three-dimensional micro-single photon emission computed tomography imaging enabling longitudinal follow-up. Liver Int. 2010;30:1211–20.
40. Wu C, van der Have F, Vastenhouw B, Dierckx RAJO, Paans AMJ, Beekman FJ. Absolute quantitative total-body small-animal SPECT with focusing pinholes. Eur J Nucl Med Mol Imaging. 2010;37:2127–35.
41. Hoeben BAW, Molkenboer-Kuenen JDM, Oyen WJG, Peeters WJM, Kaanders JHAM, Bussink J, et al. Radiolabeled cetuximab: dose optimization for epidermal growth factor receptor imaging in a head-and-neck squamous cell carcinoma model. Int J Cancer. 2011;129:870–8.
42. De Vos F, De Bruyne S, Wyffels L, Boos TL, Staelens S, Deleye S, et al. In vivo evaluation of [(123)I]-4-(2-(bis(4-fluorophenyl)methoxy)ethyl)-1-(4-iodobenzyl)piperidine, an iodinated SPECT tracer for imaging the P-gp transporter. Nucl Med Biol. 2010;37:469–77.
43. Vangestel C, Van de Wiele C, Mees G, Mertens K, Staelens S, Reutelingsperger C, et al. Single-photon emission computed tomographic imaging of the early time course of therapy-induced cell death using technetium 99m tricarbonyl His-annexin A5 in a colorectal cancer xenograft model. Mol Imaging. 2012;11:135–47.
44. Vangestel C, Van de Wiele C, Van Damme N, Staelens S, Pauwels P, Reutelingsperger CP, et al. (99)mTc-(CO)(3) His-annexin A5 micro-SPECT demonstrates increased cell death by irinotecan during the vascular normalization window caused by bevacizumab. J Nucl Med. 2011;52:1786–94.
45. Vervoort L, Burvenich I, Staelens S, Dumolyn C, Waegemans E, Van Steenkiste M, et al. Preclinical evaluation of monoclonal antibody 14C5 for targeting pancreatic cancer. Cancer Biother Radiopharm. 2010;25:193–205.
46. Blanckaert P, Burvenich I, Staelens S, De Bruyne S, Moerman L, Wyffels L, et al. Effect of cyclosporin A administration on the biodistribution and multipinhole muSPECT imaging of [123I] R91150 in rodent brain. Eur J Nucl Med Mol Imaging. 2009;36:446–53.
47. Mok GSP, Yu JH, Du Y, Wang YC, Tsui BMW. Evaluation of a multi-pinhole collimator for imaging small animals with different sizes. Mol Imaging Biol. 2012;14:60–9.
48. Goins BA, Soundararajan A, Bao A, Phillips WT, Perez R. [(186)Re]Liposomal doxorubicin (Doxil): in vitro stability, pharmacokinetics, imaging and biodistribution in a head and neck squamous cell carcinoma xenograft model. Nucl Med Biol. 2009;36:515–24.
49. Phillips WT, Head HW, Dodd GD, Bao A, Soundararajan A, Garcia-Rojas X, et al. Combination radiofrequency ablation and intravenous radiolabeled liposomal doxorubicin: imaging and quantification of increased drug delivery to tumors. Radiology. 2010;255:405–14.
50. Lin K, Hsiao I-T, Wietholt C, Chung Y, Chen C, Yen T. Performance evaluation of an animal SPECT using modified NEMA standards. J Nucl Med. 2008;49 Suppl 1:402P.
51. Schramm NU, Lackas C, Hoppin JW, Forrer F, de Jong M. The NanoSPECT/CT: a high-sensitivity small-animal SPECT/CT with submillimeter spatial resolution. Eur J Nucl Med Mol Imaging. 2006;47: Supl 1:233P.
52. Schramm NU, Lackas C, Gershman B, Norenberg JP, de Jong M. Improving resolution, sensitivity and applications for the NanoSPECT/CT: a high-performance SPECT/CT imager for small-animal research. Eur J Nucl Med Mol Imaging. 2007;34: S226–7.
53. Gershman B, Hoppin J, Schramm N, Lackas C, Norenberg J. Evaluation of the quantification capabilities of a NanoSPECT/CT as a function of angular sampling, counting statistics, reconstruction parameters and the dynamic range of measured activity. J Nucl Med. 2007;48:433P.
54. Pesnel S, Guminski Y, Pillon A, Lerondel S, Imbert T, Guilbaud N, et al. (99m)Tc-HYNIC-spermine for imaging polyamine transport system-positive tumours: preclinical evaluation. Eur J Nucl Med Mol Imaging. 2011;38:1832–41.
55. McLarty K, Cornelissen B, Cai Z, Scollard DA, Costantini DL, Done SJ, et al. Micro-SPECT/CT with 111In-DTPA-pertuzumab sensitively detects trastuzumab-mediated HER2 downregulation and tumor response in athymic mice bearing MDA-MB-361 human breast cancer xenografts. J Nucl Med. 2009;50:1340–8.

56. National Electrical Manufacturers Association. Standards Publication NU 1–2007. Rosslyn: National Electrical Manufacturers Association; 2007.
57. National Electrical Manufacturers Association. Performance measurements of positron emission tomographs. Rosslyn: National Electrical Manufacturers Association; 2001.
58. Branderhorst W, Vastenhouw B, Beekman FJ. Pixel-based subsets for rapid multi-pinhole SPECT reconstruction. Phys Med Biol. 2010;55:2023–34.
59. Van Holen R, Staelens S, Vandenberghe S. Tomographic image quality of rotating slat versus parallel hole-collimated SPECT. Phys Med Biol. 2011;56:7205–22.
60. Harteveld AA, Meeuwis AP, Disselhorst JA, Slump CH, Oyen WJ, Boerman OC, et al. Using the NEMA NU 4 PET image quality phantom in multipinhole small-animal SPECT. J Nucl Med. 2011;52:1646–53.
61. Visser EP, Harteveld AA, Meeuwis AP, Disselhorst JA, Beekman FJ, Oyen WJ, et al. Image quality phantom and parameters for high spatial resolution small-animal SPECT. J Nucl Med. 2011;52:1646–53.
62. DiFilippo FP, Gallo SL, Klatte RS, Patel S. A fillable micro-hollow sphere lesion detection phantom using superposition. Phys Med Biol. 2010;55:5363–81.
63. Liow JS, Strother SC. The convergence of object dependent resolution in maximum-likelihood based tomographic image-reconstruction. Phys Med Biol. 1993;38:55–70.
64. Wilson DW, Tsui BM, Barrett HH. Noise properties of the EM algorithm: II. Monte-Carlo simulations. Phys Med Biol. 1994;39:847–71.
65. Barrett HH, Wilson DW, Tsui BM. Noise properties of the EM algorithm: I. Theory. Phys Med Biol. 1994;39:833–46.
66. Mok GS, Wang Y, Tsui BM. Quantification of the multiplexing effects in multi-pinhole small animal SPECT: a simulation study. IEEE Trans Nucl Sci. 2009;56:2636–43.
67. Magota K, Kubo N, Kuge Y, Nishijima KI, Zhao S, Tamaki N. Performance characterization of the Inveon preclinical small-animal PET/SPECT/CT system for multimodality imaging. Eur J Nucl Med Mol Imaging. 2011;38:742–52.
68. Boisson F, Zahra D, Parmar A, Meikle S, Rellbac A. Mouse imaging capabilities of the Inveon SPECT system using single and multi-pinhole collimators dedicated to mouse studies. World Molecular Imaging Congress. 2012. Abstract P139.
69. Meikle SR, Kench P, Kassiou M, Banati RB. Small animal SPECT and its place in the matrix of molecular imaging technologies. Phys Med Biol. 2005;50:R45–61.

Contributions

S.D. performed and analysed the experiments, took part in the phantom design and construction, contributed to the writing and made all the figures. R.V.H. performed the X-SPECT experiments, contributed to the phantom design, the experimental setup and proofreading. J.V. took part in the experimental setup, image analysis and proofreading. S.V.D.B. contributed to the initial experimental setup and took part in the proofreading. Si.St. provided the motivation for the introduction of μSPECT for the investigation of antibodies and peptides in preference to μPET and contributed to the proofreading, St.St. set up the framework, originated and contributed to the phantom design, designed the experimental setups, and took part in the writing, discussion and proofreading.